





RESEARCH ARTICLE

High-resolution creatine mapping of mouse brain at 11.7 T using non-steady-state chemical exchange saturation transfer

Lin Chen^{1,2} | Zhiliang Wei^{1,2} | Shuhui Cai³  | Yuguo Li^{1,2} | Guanshu Liu^{1,2}  |
Hanzhang Lu^{1,2}  | Robert G. Weiss^{1,4} | Peter C.M. van Zijl^{1,2} | Jiadi Xu^{1,2} 

¹Russell H. Morgan Department of Radiology and Radiological Science, Johns Hopkins University School of Medicine, Baltimore, Maryland, USA

²F. M. Kirby Research Center for Functional Brain Imaging, Kennedy Krieger Research Institute, Baltimore, Maryland, USA

³Department of Electronic Science, Fujian Provincial Key Laboratory of Plasma and Magnetic Resonance, Xiamen University, Xiamen, China

⁴Division of Cardiology, Department of Medicine, Johns Hopkins University School of Medicine, Baltimore, Maryland, USA

Correspondence

Jiadi Xu, PhD, Kennedy Krieger Institute, Johns Hopkins University School of Medicine, 707 N. Broadway, Baltimore, MD 21205, USA.

Email: xuj@kennedykrieger.org

Shuhui Cai, PhD, Department of Electronic Science, Fujian Provincial Key Laboratory of Plasma and Magnetic Resonance, Xiamen University, Xiamen, China.

Email: shcai@xmu.edu.cn

Funding information

National Natural Science Foundation of China, Grant/Award Number: 11474236

The current study aims to optimize the acquisition scheme for the creatine chemical exchange saturation transfer weighted (CrCESTw) signal on mouse brain at 11.7 T, in which a strong magnetization transfer contrast (MTC) is present, and to further develop the polynomial and Lorentzian line-shape fitting (PLOF) method for quantifying CrCESTw signal with a non-steady-state (NSS) acquisition scheme. Studies on a Cr phantom with cross-linked bovine serum albumin (BSA) as well as on mouse brain demonstrated that the maximum CrCESTw signal was reached with a short saturation time determined by the rotating frame relaxation time of the MTC pool instead of the steady-state saturation. The saturation power for the maximal signal was around 1–1.5 μ T for Cr with 20% cross-linked BSA and in vivo applications, but 2 μ T was found to be most practical for signal stability. For the CrCEST acquisition with strong MTC interference, the optimal saturation power and length are completely different from those on Cr solution alone. This observation could be explained well using $R_{1\rho}$ theory by incorporating the strong MTC pool. Finally, a high-resolution Cr map was obtained on mouse brain using the PLOF method with the NSS CEST acquisition and a cryogenic coil. The Cr map obtained by CEST showed homogenous intensity across the mouse brain except for regions with cerebrospinal fluid.

KEYWORDS

chemical exchange saturation transfer (CEST), creatine, magnetization transfer, polynomial and Lorentzian line-shape fitting (PLOF)

1 | INTRODUCTION

Chemical exchange saturation transfer (CEST) MRI is a novel molecular imaging technique that has the potential to detect low concentration proteins and metabolites in vivo through the water signal.^{1–6} Since the first discovery of the CEST phenomenon about two decades ago,⁷ this technique has been successfully applied to detect pathological chemical changes in many neurological and oncological diseases,^{8–19} as well as various metabolites in tissues.^{20–24} However, a major problem hampering the widespread application of CEST is the limited specificity due to the spectral overlap of CEST signals from proteins and metabolites. The conventional CEST quantification method for creatine (Cr) is based on magnetization transfer ratio asymmetry analysis,^{25,26} ie subtracting the labeling and control water saturation images acquired at the two symmetric offsets with

Abbreviations: BSA, bovine serum albumin; CEST, chemical exchange saturation transfer; Cr, creatine; CrCESTw, creatine chemical exchange saturation transfer weighted; CSF, cerebrospinal fluid; CW, continuous wave; DS, direct water saturation; FOV, field of view; GM, gray matter; MTC, magnetization transfer contrast; NSS, non-steady-state; PCr, phosphocreatine; PLOF, polynomial and Lorentzian line-shape fitting; ppm, parts per million; RAREVTR, RARE with variable T_R ; ROI, region of interest; SNR, signal-to-noise ratio; WASSR, water saturation shift referencing; WM, white matter

respect to water resonance. However, the water saturation spectrum (Z spectrum) also contains multiple signal components that are not related to Cr, such as the relayed nuclear Overhauser enhancement (rNOE)-CEST signals at -1.6 parts per million (ppm)²⁷ and around -3.5 ppm,^{21,28} as well as the magnetization transfer contrast (MTC) with slow exchanging rate also centered about -3.5 ppm.^{21,28} Therefore, the asymmetry analysis results may introduce contaminations from lipids, proteins, semisolid macromolecules and other metabolites. Several other CEST quantification methods, such as the chemical exchange rotation transfer technique,²⁹⁻³¹ the Lorentzian line-shape fitting method^{14,15,32} and the off-resonance variable-delay multiple-pulse method,²⁸ have been proposed to extract CEST signal with improved specificity to some extent, eg by partially removing the MTC and direct water saturation (DS)^{12,15} and avoiding or removing the contaminations from the aliphatic CEST signals. However, these methods still face the difficulty of removing interference from other CEST peaks, such as the broad peaks from aromatic, fast-exchanging amine and hydroxyl protons. Recently, a combined polynomial and Lorentzian line-shape fitting (PLOF) that removes broad CEST background signals was proposed to extract and quantify Cr and phosphocreatine (PCr).^{33,34} A similar strategy was also implemented by a different group for PCr mapping with CEST.³⁵ The successful application of PLOF requires sufficient signal-to-noise ratio (SNR) and image stability as do other CEST quantification methods. However, the previous PLOF studies indicate that the Cr CEST-weighted (CrCESTw) signal is seriously scaled down by the competing strong MTC background, resulting in less than 1.5% of water signal under steady-state conditions at 11.7 T.^{33,36} Therefore, further possibilities of improving the SNR need to be explored, ie either reducing the scale-down effect or reducing the noise in the Z spectrum.

It is well known that CEST effects reduce with the presence of MTC.^{12,37-39} In this study, we derived the relationship between saturation length and observed CEST signal with the presence of strong MTC background and found that the maximum observed CEST signal is achieved at non-steady-state (NSS) saturation. This finding was validated on phantoms of Cr mixed with cross-linked bovine serum albumin (BSA) as well as in vivo in wild type mouse brain. The PLOF method was thus extended for quantification of CrCESTw signal under NSS situations.

2 | THEORY

2.1 | CEST with strong MTC background

According to the previous studies, the observed CEST signal in tissues is significantly affected by the strong MTC background.^{33,37,38} For continuous wave (CW) saturation, the CEST signal can be well explained by $R_{1\rho}$ theory,³⁹⁻⁴⁴ which we used to obtain analytical equations for the CEST signal with multiple exchanging pools. The normalized saturation signal Z (ie the water saturation signal S normalized by the signal without saturation S_0) at each offset is given by^{39,40,43,44}

$$Z(R_{1\rho}) = (1 - Z^{ss})e^{-R_{1\rho}t_{sat}} + Z^{ss} \quad (1)$$

$$Z^{ss} = \frac{\cos^2 \theta R_1}{R_{1\rho}} \quad (2)$$

where Z^{ss} is the steady-state Z-spectral intensity, R_1 is the longitudinal relaxation rate of water, t_{sat} is the saturation time, and $\theta = \tan^{-1}\omega_1/\Delta$ is the tilt angle of the effective magnetization with respect to the Z-axis induced by a saturation pulse with nutation frequency ω_1 at an offset Δ . $R_{1\rho}$ is the water relaxation rate under the saturation pulse, which includes contributions from the effective water relaxation R_{eff} and an apparent relaxation term R_{ST} related to all saturation transfer processes in tissue⁴³:

$$R_{1\rho} = R_{eff} + R_{ST} \quad (3)$$

where $R_{eff} = \cos^2 \theta R_1 + \sin^2 \theta R_2$ is the measured longitudinal relaxation rate of water in the rotating frame without additional solution components. Under steady-state conditions, ie $t_{sat} > 3/R_{1\rho}$, the observed Z spectrum is related to $R_{1\rho}$ through Equation 2, which has been widely used in the CEST field for inverse metric evaluations.^{31,45-49} The benefit of using $R_{1\rho}$ for CEST quantification is that $R_{1\rho}$ is reflective of and proportional to the concentration of the exchanging protons. Hence, all the saturation transfer components can be linearly superimposed under the framework of $R_{1\rho}$.^{33,38,44} In the current study, a two-pool model consisting of a guanidinium pool from both Cr and protein plus a background pool reflecting all the other contributing protons was used to analyse the CEST signal, giving

$$R_{ST} = R_{back} + R_{guan} \quad (4)$$

The observed CEST signal ΔZ is given by

$$\Delta Z = Z(R_{back}) - Z(R_{back} + R_{guan}) \quad (5)$$

For the in vivo CrCESTw experiment at typical B_1 values used ($0 \mu T$ to $2 \mu T$), R_{guan} is much smaller than R_{back} (ie, $R_{guan} \ll R_{back}$) due to the strong MTC contribution. Then ΔZ can be divided into two terms, ΔZ_1 and ΔZ_2 (see the appendix for details).

$$\Delta Z = \Delta Z_1 + \Delta Z_2 \quad (6)$$

$$\Delta Z_1 = \Delta Z^{ss} (1 - e^{-R_{1p} t_{sat}}) \quad (7)$$

$$\Delta Z_2 = (1 - Z^{ss}) t_{sat} R_{guan} e^{-R_{1p} t_{sat}} \quad (8)$$

where the steady-state CEST signal ΔZ^{ss} is given by

$$\Delta Z^{ss} \approx Z^{ss2} (1 - Z_{guan}^{ss}) \quad (9)$$

or

$$\Delta Z^{ss} = \frac{\cos^2 \theta R_{guan} R_1}{R_{1p}^2} \quad (10)$$

ΔZ as a function of saturation time in the presence of a strong background signal (R_{back}) is simulated in Figure 1. The two CEST terms, ΔZ_1 and ΔZ_2 , are included for comparison. ΔZ_1 is the typical CEST buildup curve when a single CEST pool is considered, which has been well studied previously. As seen from Equation 9, ΔZ_1 is scaled down by a factor of Z^{ss2} , as demonstrated in the previous studies.^{33,34} ΔZ_2 is usually neglected in the CEST studies since it is zero under steady-state saturation. However, this term becomes significant when the MTC is strong, ie Z^{ss} is much smaller than one, and the saturation time is short as seen from Equation 8. ΔZ_2 is a buildup and decay curve as a function of saturation length (t_{sat}) with the maximum value at (Figure 1B)

$$t_{sat} = \frac{1}{R_{back} + R_{eff}} \quad (11)$$

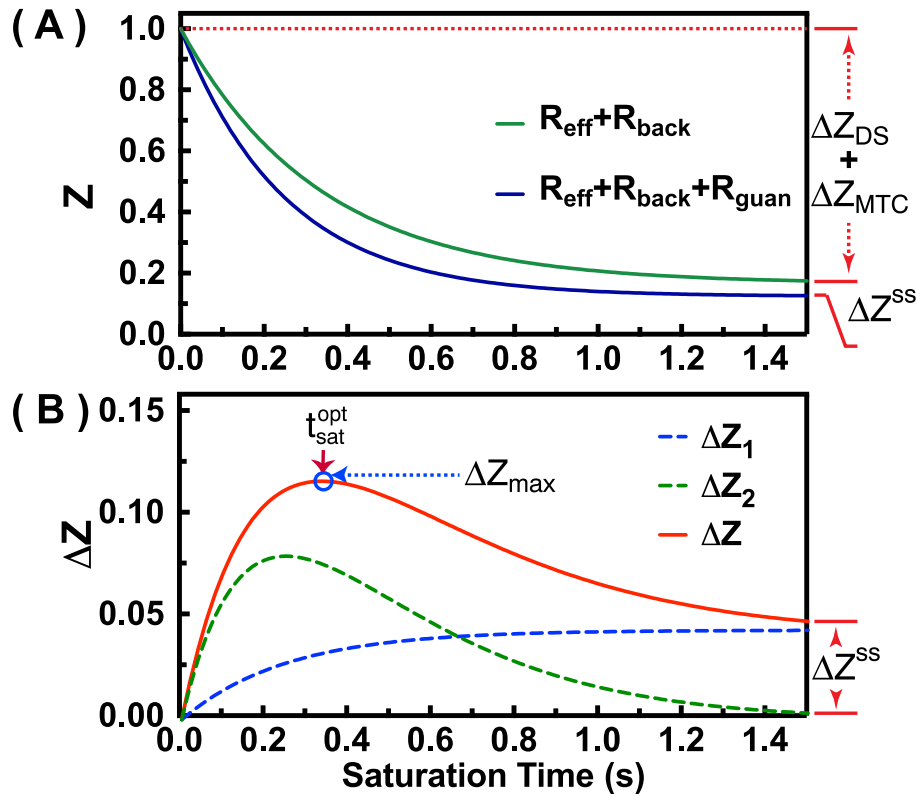


FIGURE 1 Illustration of the Z value (a) and the corresponding CEST signal (ΔZ) (b) as a function of saturation time in the presence of strong MTC. The simulation was performed using equation 1 by assuming $\cos^2 \theta = 1$, $R_1 = 0.5 \text{ s}^{-1}$, $R_{back} = 3.0 \text{ s}^{-1}$ and $R_{guan} = 1.0 \text{ s}^{-1}$. In order to illustrate the guanidinium CEST signal, a R_{guan} value that is much higher than the typical in vivo values ($<0.1 \text{ s}^{-1}$) was used. The steady-state CEST (ΔZ^{ss}), MTC (ΔZ_{MTC}) and DS (ΔZ_{DS}) signal contributions are indicated in a and are generated by R_{guan} , R_{back} and R_{eff} , respectively. The optimum saturation time (t_{sat}^{opt}) at which the CEST signal (ΔZ_{max}) reaches maximum is indicated in B

When combining ΔZ_1 and ΔZ_2 , the maximum CEST signal ΔZ will be obtained at a short saturation time (around $1/R_{1\rho}$) instead of at steady state (Figure 1B).

2.2 | PLOF scheme for extracting and quantifying CrCESTw signal

A PLOF scheme was designed to extract R_{guan} from the Z spectrum and use this value to quantify Cr concentrations based on the theory that R_{guan} is proportional to the Cr concentration.^{33,34} The Z spectrum between 1 and 3 ppm contains two major components: a well defined guanidinium peak (R_{guan}), and a broad background signal (R_{back}) including DS, MTC, aromatic protons and other metabolites. These two components can be represented as a Lorentzian function and a polynomial function, respectively:

$$R_{\text{guan}} = R_{\text{guan}}^{\text{max}} \frac{(w/2)^2}{(w/2)^2 + (\Delta - \Delta_{\text{guan}})^2} \quad (12)$$

$$R_{\text{back}} = C_0 + C_1(\Delta - \Delta_{\text{guan}}) + C_2(\Delta - \Delta_{\text{guan}})^2 + C_3(\Delta - \Delta_{\text{guan}})^3 \quad (13)$$

where w is the peak full-width at half-maximum of the Lorentzian line-shape. $R_{\text{guan}}^{\text{max}}$ is the true apparent relaxation rate contribution of the guanidinium protons. Δ_{guan} is the chemical shift of the guanidinium peak, which is around 1.95 ppm in vivo; terms C_0 to C_3 are the zeroth- to third-order polynomial coefficients.

The PLOF Cr mapping includes the following steps.

- i. Fitting Z_{back} without the guanidinium CEST peak, ie, $R_{\text{guan}}^{\text{max}} = 0$ in Equation 12 for each pixel as shown in Figure 2A. The background $Z(R_{\text{back}})$ was fitted by excluding the data points between 1.6 ppm and 2.4 ppm and varying the parameters C_0 - C_3 in R_{back} (Equation 13). The range selected for background fitting was determined from power dependent Z spectra recorded on a Cr + 20% BSA phantom and the mouse brain. Here, R_{back} was assumed to be a polynomial function instead of Z_{back} as used in our previous study.³³ With the new definition, we found a third-order polynomial function is sufficient to fit the background signal. Extracting the R_{guan} peak of guanidium (1.95 ppm in mouse brain or 2 ppm for Cr phantom) from the Z spectrum with a fixed R_{back} for each pixel (Figure 2B). The complete Z-spectral data $Z(R_{\text{back}} + R_{\text{guan}})$ were fitted by varying the parameters w , Δ_{guan} and $R_{\text{guan}}^{\text{max}}$ in Equation 12; the Z-spectrum difference between $Z(R_{\text{back}})$ and $Z(R_{\text{back}} + R_{\text{guan}})$ at the offset

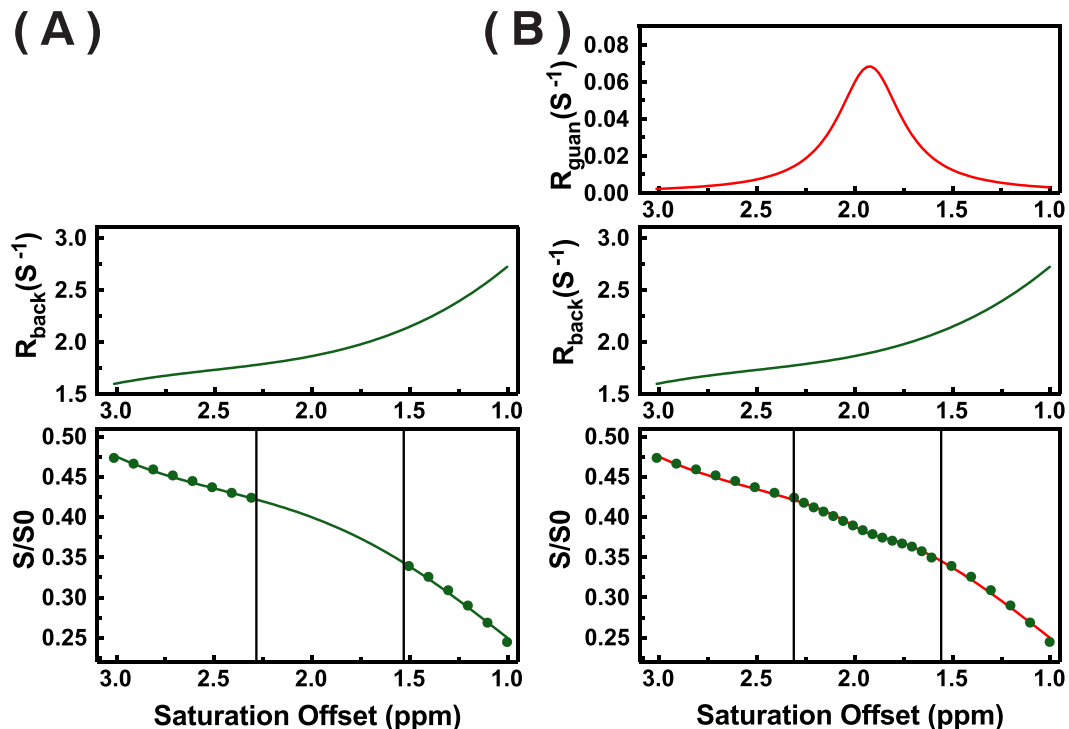


FIGURE 2 Illustration of the PLOF scheme for extracting the CEST signal from the in vivo Z spectrum. A two-step fitting procedure was applied. A, first, the background Z spectrum R_{back} (ie outside the range between 1.6 ppm and 2.4 ppm) was fitted using equation 1. The measured R_1 values were included in this fitting, and R_{back} was obtained by varying the parameters C_0 - C_3 in equation 13. B, after the background fitting, all Z-spectral data were fitted by varying the R_{guan} values with fixed R_{back} . The R_{guan} values were determined using equation 12

of 2 ppm (Cr phantom) or 1.95 ppm (brain), ie $\Delta Z_{\text{guan}}^{\text{max}}$ is the observed guanidinium CEST signal and will thus be used for the optimization of the acquisition parameters.

- ii. Translating the extracted R_{guan} map into a Cr concentration map using the calibration curve obtained by ^1H MRS. The fitted $R_{\text{guan}}^{\text{max}}$ map of the mouse brain can be correlated to the Cr concentration by the following relationship³³:

$$R_{\text{guan}}^{\text{max}} = R_{\text{protein}} + r_{\text{Cr}}[\text{Cr}] \quad (14)$$

where R_{protein} indicates the guanidinium contribution from mobile proteins and r_{Cr} is the apparent spin-lock relaxivity (expressed in $\text{s}^{-1}\text{mM}^{-1}$) of Cr, which is analogous to the relaxivity term used for contrast agent studies. The protein contribution is difficult to obtain. For the healthy brain, we assume that the ratio of R_{protein} and $R_{\text{guan}}^{\text{max}}$ is constant considering that both Cr and protein are constant across mouse brain; Equation 14 can then be rewritten as

$$R_{\text{guan}}^{\text{max}}\lambda = r_{\text{Cr}}[\text{Cr}] \quad (15)$$

where λ is the ratio between Cr and protein signal in R_{guan} . r_{Cr} can be obtained using a calibration curve measured with in vivo MRS. Note that in the cases where the ratio between R_{protein} and $R_{\text{guan}}^{\text{max}}$ cannot be regarded as constant, only a relative Cr concentration variation can be obtained using Equation 14.

3 | METHODS

3.1 | Phantom preparation

Four phantoms were prepared, a Cr (50mM) solution and Cr (50mM) solutions mixed with 5%, 10% and 20% cross-linked BSA (Cr + 5% BSA, Cr + 10% BSA and Cr + 20% BSA). BSA was utilized to mimic the strong background signal commonly seen in in vivo tissue. BSA crosslinking was achieved using $25 \mu\text{L mL}^{-1}$ glutaraldehyde solution. Phantoms were prepared in phosphate buffered saline, titrated to pH 7.3. All phantoms were studied in 5 mm NMR tubes and maintained at 37°C during MRI experiments using an air heater.

3.2 | Animal preparation

All animal experiments were performed according to the protocols approved by the Institutional Animal Care and Use Committee at Johns Hopkins University. Six adult female BALB/c mice (6 months) were used for the experiments. All animals were induced using 2% vaporized inhaled isoflurane, followed by 1.5% isoflurane during the MRI scan.

3.3 | MRI

All MRI experiments were performed on a horizontal bore 11.7 T Bruker BioSpec system (Bruker, Ettlingen, Germany). A 23 mm volume transceiver coil was used for all the phantom studies. For in vivo experiments, a 72 mm quadrature volume resonator was used as a transmitter, and a cryogenic 2×2 phased array coil (CryoProbe from Bruker, Ettlingen, Germany) as a receiver. The CEST experiments were performed using a CW-CEST saturation pulse before the MRI readout.

3.3.1 | Experiment I. the impact of macromolecules on the CrCEST signal

Cr phantoms (50mM) mixed with different concentrations of cross-linked BSA (5%, 10% and 20%) were used to demonstrate the spillover effects on CEST signal due to the presence of MTC. They were also used to examine the impact of cross-linked BSA on the Cr properties, such as the proton exchange rate and the binding of Cr molecules to BSA, which are supposed to be correlated with the BSA concentration. The saturation offset was swept from 1 ppm to 3 ppm with an increment of 0.1 ppm to record Z spectra using a CW-CEST sequence and a RARE readout. A saturation power of $2 \mu\text{T}$ (5 s saturation length) was used. The slice thickness was 2 mm, the field of view (FOV) was $15 \times 15 \text{ mm}^2$ and the matrix size was 64×64 .

3.3.2 | Experiment II. Optimization of saturation power and length on Cr phantoms

For the saturation power optimization, the CW-CEST experiments were performed on the Cr and Cr + 20% BSA phantoms with a fixed saturation time of 2 s, while the saturation power was varied from 0.4 to $3 \mu\text{T}$. The saturation offset ranged from 1 to 3 ppm with 0.1 ppm increment. The

RARE MRI readout was identical to that used in Experiment I. The Cr signal (ΔZ_{Cr}) in cross-linked BSA was extracted using the PLOF method as detailed above, and ΔZ_{Cr} in Cr solution alone was calculated by subtracting the Z spectrum at 2 ppm (Z(2 ppm)) from unity, ie, $\Delta Z_{Cr} = 1 - Z(2 \text{ ppm})$. T_1 maps were measured using a RAREVTR sequence (RARE with variable $T_R = 0.5, 1, 1.5, 2, 3.5, 5, 8 \text{ s}$).

For the saturation length optimization on Cr phantoms, the saturation power was fixed at 2 μT or 4 μT , while the saturation length was varied from 0.5 s to 5 s for 2 μT saturation power and 0.2 s to 2 s for 4 μT saturation power.

3.3.3 | Experiment III. Optimization of saturation length on mouse brain

The saturation length for CEST acquisition on mouse brain was optimized with two saturation powers (1 μT and 2 μT). The saturation offset swept from 1 to 3 ppm with an increment of 0.1 ppm to record the Z spectrum, and a 0.05 ppm increment between 1.6 ppm and 2.4 ppm was added, which leads to a total scan time of 5 min per Z spectrum. The B_0 field was adjusted with up to second-order shimming using field-mapping prior to the study. A water saturation shift referencing (WASSR) method was applied to check the B_0 map after the shimming.⁵⁰ The R_{back} value at the offset of 1.95 ppm was obtained by fitting the saturation time dependent Z value according to Equation 1. The slice thickness was 1.5 mm, the FOV was $15 \times 15 \text{ mm}^2$ and the matrix size was 32×32 .

3.3.4 | Experiment IV. High-resolution Cr map on mouse brain

Based on the optimization results, a saturation module with 2 μT saturation power and 1 s saturation length was applied to acquire a high-resolution Cr map. From our previous study on skeletal muscle at the same MRI field and saturation power, the PCrCEST signal at 2.6 ppm is 16.4% of CrCESTw at 1.95 ppm,^{33,34} and the PCrCEST signal at 1.95 ppm is 55% of the PCr signal at 2.6 ppm.^{33,35,51} In the muscle, the PCr concentration is three times the Cr concentration, while the PCr and Cr concentrations are comparable in brain.⁵²⁻⁵⁶ Therefore, the PCr contribution to the CEST signal at 1.95 ppm in the brain was assumed to be small (<10%). The saturation offsets were identical to those applied in Experiment II. A RARE readout was applied for the Cr mapping. The slice thickness was 1.5 mm, the FOV was $15 \times 15 \text{ mm}^2$ and the matrix size was 64×64 . T_1 maps were acquired using the same geometry and spatial resolution as CEST MRI using a RAREVTR sequence identical to that used for the phantom T_1 measurement. The T_1 map is needed for Cr quantification with the PLOF method. The Cr concentration in mouse brain was determined from in vivo proton MRS experiments, which were performed on a voxel of $2 \times 2 \times 2 \text{ mm}^3$ using a stimulated echo acquisition mode (STEAM) sequence ($T_E = 3 \text{ ms}$, $T_M = 10 \text{ ms}$, $T_R = 2.5 \text{ s}$, number of average (NA) = 256).³³

3.4 | Data analysis

A non-linear least square fitting algorithm was applied in the PLOF method using the MATLAB built-in function lsqcurvefit. The initial chemical shift of the guanidinium peak was set to 1.95 ppm, and its lower bound and upper bound were 1.8 ppm and 2.1 ppm, respectively. Brain Cr concentrations measured using in vivo ^1H MRS spectra were estimated using LCModel analysis as detailed in previous work.³⁴ A calibration phantom with 20mM Cr mixed with cross-linked BSA (20 wt%, pH = 7.2) was used for the calibration of the MRS quantification. One MRS spectrum was collected on the calibration phantom using acquisition parameters identical to those used for mouse brain studies. Then, the area of the Cr N-methyl peak for the phantom was quantified using LCModel.^{57,58} The total Cr (tCr = Cr + PCr) concentration was obtained from the ratio (g) between the area under a best fit tCr spectrum in the LCModel on the brain and on the calibration phantom (20mM Cr in cross-linked BSA) as $g \times 20 \text{ mM}$. The Cr and PCr concentrations were assumed to be 1:1 in the mouse brain.⁵²⁻⁵⁶ The T_1/T_2 relaxation times of water protons in the cross-linked BSA ($T_1 = 1.8 \text{ s}$ and $T_2 = 46 \text{ ms}$) were close to those of the mouse brain at 11.7 T ($T_1 = 2.0 \pm 0.2 \text{ s}$ and $T_2 = 35 \pm 4 \text{ ms}$).⁵⁹ Hence, the relaxation induced quantification error can be minimized.

4 | RESULTS

4.1 | Experiment I. the impact of macromolecules on the CrCEST signal

In Figure 3A, the Z spectra of Cr and of the Cr phantoms mixed with different concentrations of cross-linked BSA are shown. The CrCESTw peaks of the Cr + 5% BSA, Cr + 10% BSA and Cr + 20% BSA phantoms are much smaller than that of Cr solution alone. The fitted curves and fitting parameters (ΔZ , R_{guan} and R_{back}) obtained using the PLOF method are shown in Figure 3B and Table 1, respectively. It can be seen that the presence of MTC has a significant impact on the measured values of CrCEST (ΔZ). Although the concentration of Cr was identical in all phantoms (50mM), ΔZ is inversely proportional to the strength of MTC induced by cross-linked BSA. In contrast to ΔZ , R_{guan} showed robustness, which is a desirable property for quantification of Cr. The similarity of R_{guan} values for all phantoms also indicates that the cross-linked BSA had a negligible effect on the Cr exchanging properties.

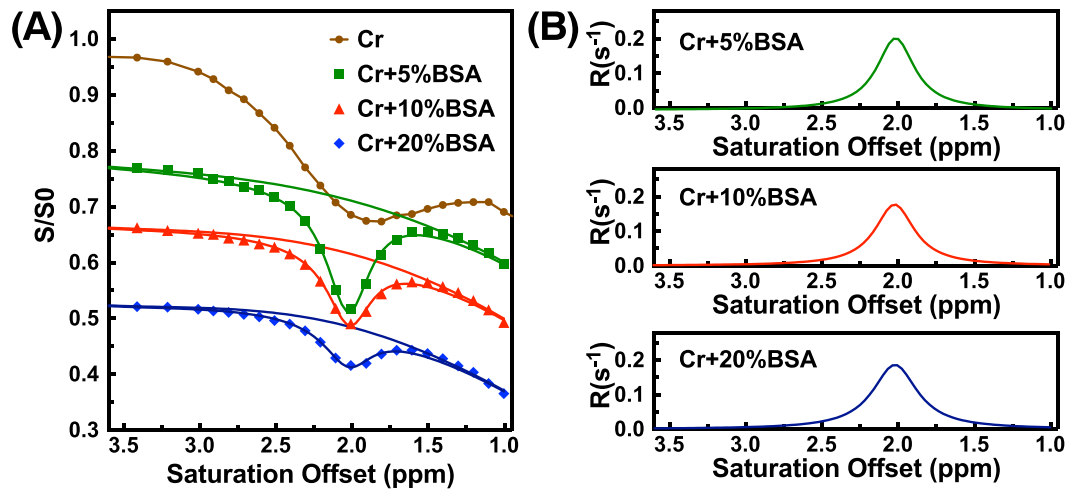


FIGURE 3 The scaling-down effect of the CrCEST signal in the presence of MTC, and the corresponding R_{guan} curves fitted using the PLOF method. The saturation power was 2 μT and the saturation length was 5 s. a, the Z spectra of Cr, Cr + 5% BSA, Cr + 10% BSA and Cr + 20% BSA. The fitted Z spectra and fitted background for the phantoms with Cr + 5% BSA, Cr + 10% BSA and Cr + 20% BSA. The parameters used for the fitting are listed in Table 1. B, the obtained R_{guan} curves for the Cr phantoms with cross-linked BSA (5%, 10% and 20%)

TABLE 1 The measured T_1 values used for the PLOF fitting method, and the obtained ΔZ , R_{back} and R_{exch} values on the Cr phantoms shown in Figure 3

Sample	T_1 (s^{-1})	ΔZ	R_{back} (s^{-1})	R_{exch} (s^{-1})
Cr	2.75 ± 0.05	0.31 ± 0.02	0	0.16 ± 0.02
Cr + 5% BSA	2.65 ± 0.05	0.19 ± 0.02	0.55 ± 0.03	0.20 ± 0.02
Cr + 10% BSA	2.38 ± 0.04	0.12 ± 0.01	0.69 ± 0.05	0.17 ± 0.02
Cr + 20% BSA	1.91 ± 0.03	0.06 ± 0.01	1.08 ± 0.05	0.17 ± 0.02

4.2 | Experiment II. Saturation length and power optimization on Cr phantoms

Figure 4 shows the Z spectra of Cr and Cr + 20% BSA recorded with different saturation powers. The power dependent CEST signal of Cr in solution is obviously different from that of Cr in 20% BSA. For Cr solution the CEST signal (ΔZ_{Cr}) increases with saturation power, while for Cr + 20% BSA ΔZ_{Cr} first increases slowly with power but then starts to decrease, leading to a maximum ΔZ_{Cr} at around 1 μT . The decrease of ΔZ_{Cr} in Cr + 20% BSA is caused by the scaled-down effect induced by competition from MTC following Equation 9.

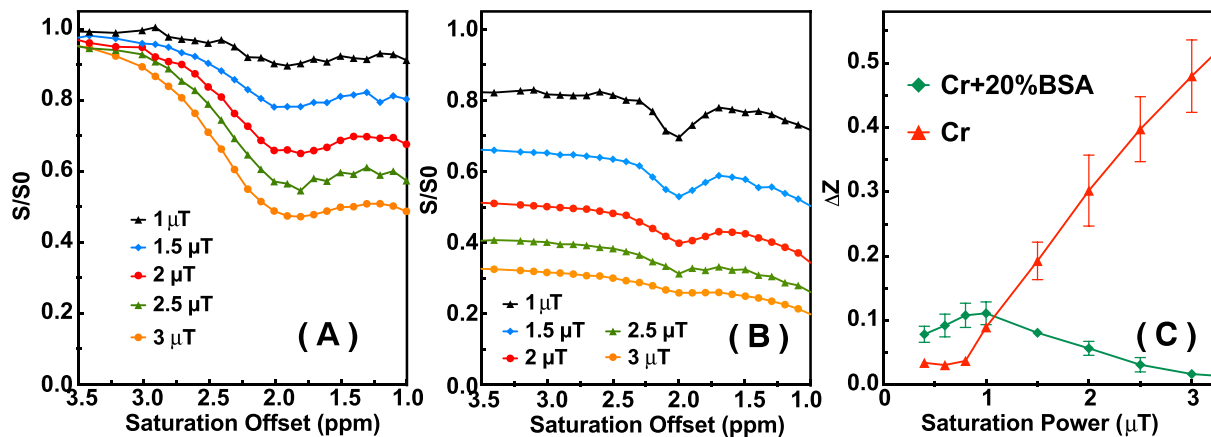


FIGURE 4 A, B, typical phantom Z spectra for solutions of Cr (a) and Cr + 20% BSA (B) as a function of saturation power with a fixed saturation length of 5 s. C, the CrCEST signal of Cr solution and Cr + 20% BSA as a function of saturation power

Figure 5 shows the Z spectra and corresponding ΔZ_{Cr} for these two phantoms as a function of saturation length. For the Cr solution (Figure 5A and 5C), ΔZ_{Cr} increases exponentially with saturation length, which is consistent with the theoretical curve predicted by Equation 1. With the interference of strong MTC, the buildup curve of ΔZ_{Cr} is completely different, as shown in Figure 5B and 5D. The ΔZ_{Cr} increases rapidly with the saturation length, levels off and then decays slowly. This pattern is similar to the simulated ΔZ curve in the presence of strong MTC in Figure 1. The solid curves in Figure 5D were fitted using Equations 6–8 with measured water relaxation time $T_1 = 1.9 \text{ s}^{-1}$, $R_{back} = 1.15 \text{ s}^{-1}$ and $R_{guan} = 0.15 \text{ s}^{-1}$ for 2 μT , and $R_{back} = 2.5 \text{ s}^{-1}$ and $R_{guan} = 0.12 \text{ s}^{-1}$ for 4 μT . For the saturation power of 4 μT , the ΔZ_{Cr} at steady state is around 0.009, which is only half of the maximum ΔZ_{Cr} (0.019) occurring at a saturation length of around 0.6 s.

4.3 | Experiment III. Optimization of saturation length on mouse brain

The evolution of Z values as a function of saturation time at 1.95 ppm for mouse brain is shown for two saturation powers in Figure 6A. The fitted buildup curves based on Equation 1 are also plotted. For the in vivo CEST experiment at this offset, MTC is the dominant contribution. The well fitted buildup curves indicate that MTC can also be approximated well by $R_{1\rho}$ theory. The $R_{1\rho} = R_{eff} + R_{back}$ can be determined from these fitted buildup curves, giving $0.96 \pm 0.01 \text{ s}^{-1}$ and $1.62 \pm 0.01 \text{ s}^{-1}$ for the saturation powers of 1 μT and 2 μT , respectively. The power dependence

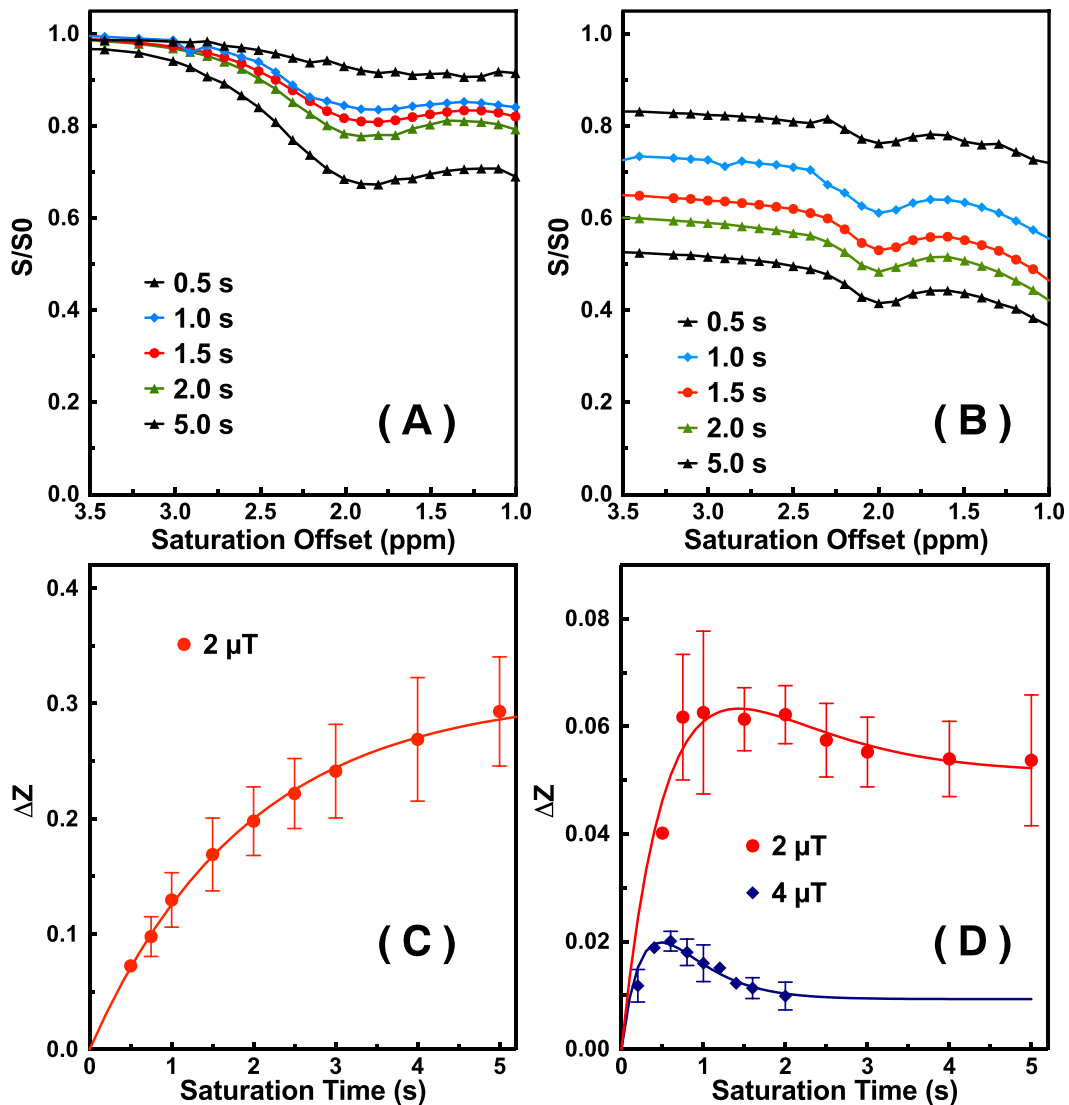


FIGURE 5 A, B, typical phantom Z-spectra of Cr (a) and Cr + 20% BSA (B) as a function of saturation length with a fixed saturation power of 2 μT . C, the saturation length dependent CrCEST signal of the Cr phantom for a saturation power of 2 μT . The solid line is the fitting curve using equation 1 with $R_{1\rho} = 0.52 \text{ s}^{-1}$. D, the saturation length dependent CrCEST signal of the Cr + 20% BSA phantom for saturation powers of 2 μT and 4 μT , respectively. Solid lines are the fitted curves using equations 6–8. In the fitting, the measured $T_1 = 1.9 \text{ s}^{-1}$ for the phantoms was used

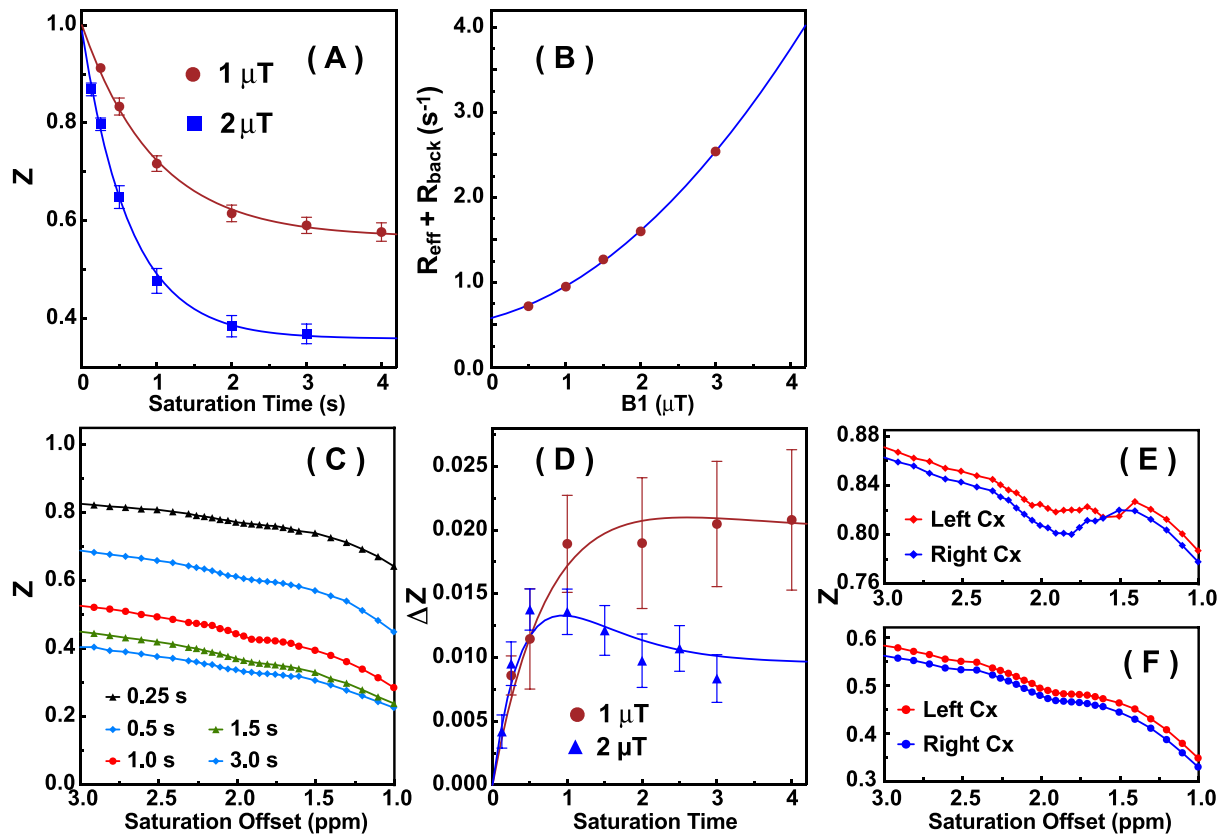


FIGURE 6 A, the saturation time dependent Z values for mouse brain at 1.95 ppm for saturation powers of 1 μT and 2 μT , respectively. The solid lines are the fitted curves using equation 1 to extract the $R_{1\rho} = R_{\text{eff}} + R_{\text{back}}$ values for each saturation power. B, the power dependent $R_{1\rho}$ values at 1.95 ppm for mouse brain. The solid line is the fitted curve with equation 16. C, typical Z spectra of mouse brain using CW-CEST with a fixed saturation power of 2 μT and varying saturation lengths. D, the guanidinium CEST (ΔZ_{guan}) intensity as a function of saturation time over whole mouse brain for saturation powers of 1 μT and 2 μT , respectively. Solid lines are the fitted curves using equations 6–8. E, F, typical Z -spectra recorded for the left and right cortex of mouse brain with 1 $\mu\text{T}/3$ s (E) and 2 $\mu\text{T}/1$ s (F) CW-CEST acquisition, respectively

of $R_{\text{eff}} + R_{\text{back}}$ is shown in Figure 6B. The relationship between $R_{\text{eff}} + R_{\text{back}}$ and saturation power can be fitted well with a second-order polynomial function:

$$R_{\text{eff}} + R_{\text{back}} = 0.58 + 0.24B_1 + 0.14B_1^2 \quad (16)$$

where B_1 refers to the saturation power in units of microtesla. The intercept (0.58 s^{-1}) is the water R_1 . Typical Z spectra recorded on mouse brain and the corresponding ΔZ values as a function of saturation time are shown in Figure 6C and D. For the saturation power of 1 μT , ΔZ increases rapidly before leveling off at around 1 s, but does not show any obvious decay as the saturation time further increases. The buildup curve for saturation power of 2 μT is similar to that of Cr + 20% BSA, first increasing and then leveling off and decaying with increasing saturation time. For this saturation power of 2 μT , ΔZ was $1.3 \pm 0.2 \times 10^{-2}$ at a saturation time of 1 s, which was about 14% higher than that at steady state (2 s). The time dependent CEST signal was fitted according to Equations 6–8, giving $R_{\text{guan}} = 0.045 \text{ s}^{-1}$ for 2 μT and $R_{\text{guan}} = 0.032 \text{ s}^{-1}$ for 1 μT , and R_{back} values determined by Equation 16 to be 1.04 s^{-1} and 0.38 s^{-1} , respectively. In Figure 6E and 6F the Z spectra of the contralateral cortices recorded with 1 μT and 2 μT are shown, indicating reduced effects but better consistency at 2 μT .

4.4 | Experiment IV. High-resolution Cr mapping of mouse brain

The tCr concentration in the thalamus was found to be $10.0 \pm 0.2 \text{ mM}$ ($n = 3$) by in vivo MRS, which leads to a Cr concentration of $5.0 \pm 0.1 \text{ mM}$, while $R_{\text{guan}}^{\text{max}}$ was determined to be $0.11 \pm 0.01 \text{ s}^{-1}$ with a saturation power of 2 μT and a saturation length of 1 s. Hence, $r_{\text{Cr}} = 0.018 \text{ s}^{-1} \text{ mM}^{-1}$ was derived according to Equation 15 by assuming $\lambda = 0.8$, in which λ is a ratio that defines Cr and protein guanidinium CEST signal at 1.95 ppm and was determined in our previous study.³³ This was then used for scaling the Cr concentration maps for the brain. A typical Cr concentration map is shown in Figure 7C. The C_0 map obtained from fitting the background signal in each voxel using Equation 13 contains contributions mainly from MTC, as confirmed by a strong contrast between white matter (WM) and gray matter (GM). Due to the scale-down effect induced by MTC, the ΔZ

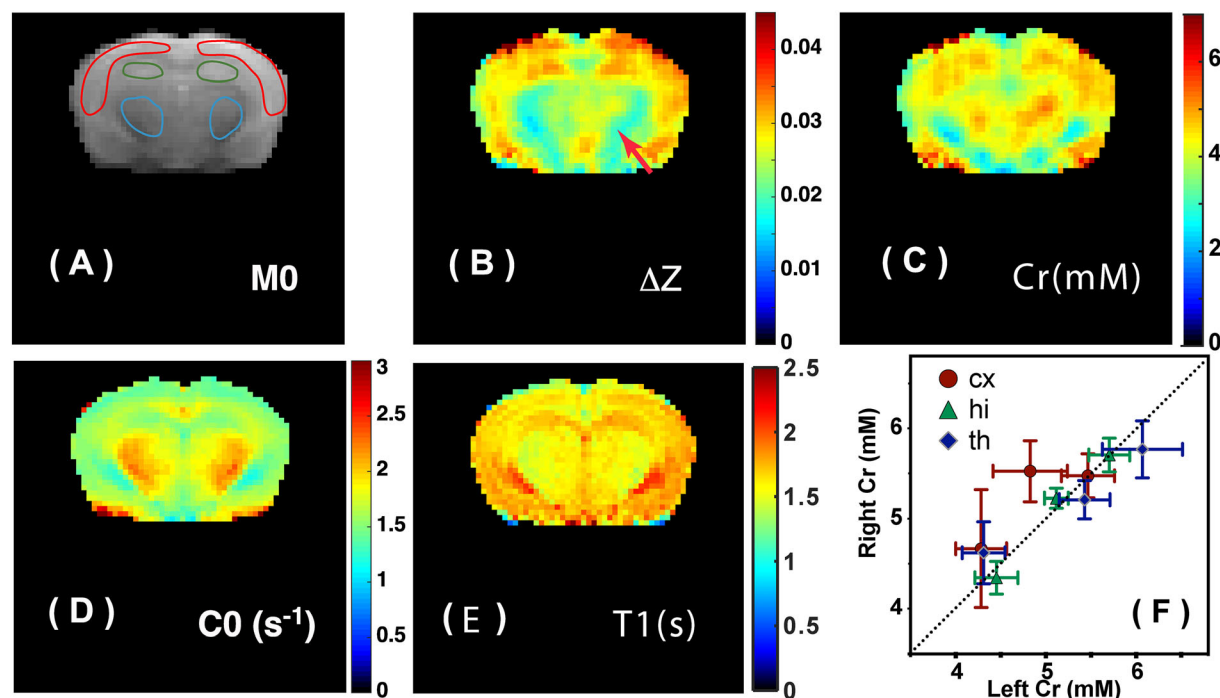


FIGURE 7 In vivo mouse brain imaging of Cr using the PLOF method. A, M0 image, B, ΔZ_{guan} map, C, Cr concentration map, D, C_0 map, and E, T_1 map. F, bilateral symmetry assessment of Cr concentrations for three brain regions illustrated in a: cortex (cx), hippocampus (hi) and thalamus (th). Results for all three mice are shown. Error bars represent the in-ROI standard derivations. The experiment was carried out using CW-CEST with 2 μT saturation power and 1 s saturation length. The maps were calculated pixel by pixel by fitting the Z spectra between 1 and 3 ppm with the PLOF method. One region seriously affected by MTC (thalamus) is indicated by a red arrow in the ΔZ_{guan} map, while a correct Cr concentration is found in C. the C_0 map contains contributions mainly from MTC and clearly shows strong WM to GM contrast, similar to conventional MTC maps

values are obviously reduced in WM regions as indicated by the red arrow in Figure 7B. Using the PLOF method the scale-down effect was eliminated, leading to homogenous intensities across the WM and GM regions. The fitting accuracy of the PLOF method was satisfactory, with an average $R^2 > 0.999$ for the whole brain. Quantitative Cr analyses were performed on three brain structures: cortex, hippocampus and thalamus. In order to assess the bilateral symmetry of Cr concentration, we plotted the left and right hemispheric concentrations for these three brain regions for all three mice in Figure 7F. The Cr concentration appears to be homogenous across the brain, with a mean value of 5.1mM for the three structures. Due to the presence of cerebrospinal fluid (CSF) compartments and partial volume effects from CSF, some regions of the brain show reduced Cr concentration. The within-ROI (region of interest) standard deviations are also plotted in the same figure and found to be around 10% of the mean Cr concentrations.

5 | DISCUSSION

The current study explored the saturation parameters and several MRI readout approaches for CEST-based Cr mapping of the mouse brain. A quantification method dubbed PLOF^{33,34} was further developed to include saturation time dependent effects, and its efficiency was verified on Cr phantoms and in vivo mouse brain. The PLOF approach is based on $R_{1\rho}$ theory and can explain the observed CrCESTw signal well with multiple pools. By correcting the scaled-down effect induced by strong MTC, the PLOF method provides a reliable way to map Cr in the mouse brain. According to our results, many experimental parameters determined to be optimal for Cr in liquid solution are not suitable in the presence of a strong MTC, such as for in vivo CEST studies. Although similar conclusions may also be obtained using the conventional Bloch-McConnell numerical equations, the analytical solution can provide more insights into the correlation between the CEST signal and the acquisition parameters. Besides, the $R_{1\rho}$ method used in this study also provides a simple way to model the MTC component. The principles proposed in this study for Cr can be applied to other CEST compounds including injected agents, and provide a needed guideline for the in vivo CEST acquisitions. For the PLOF method used in this study, the frequency offsets of 1.6 ppm and 2.4 ppm were selected as the boundary of the CrCEST peak and background region. This boundary will lead to a slightly underestimated value (around 5% reduced compared with that obtained with the boundary from 1.4 ppm to 2.6 ppm), but will improve the accuracy of the background fitting, especially in noisy situations, because more data are adopted for the background fitting. Therefore, when applying PLOF to quantify other CEST compounds or under different magnetic fields, the boundary of the CEST peak and background region need to be carefully designed to trade off the underestimation of the CEST peak and the accuracy of background fitting. In the following sections, the selection of appropriate parameters is further discussed.

5.1 | Saturation power selection

Conventionally, high saturation powers ($>3 \mu\text{T}$) are preferred when detecting CEST effects for faster-exchanging protons. This strategy works well for Cr in liquid solution, as shown in Figure 4A and 4C, where ΔZ_{Cr} increases with saturation power. When a strong competing saturation transfer effect such as MTC is present, however, which is the case for in vivo CEST applications, the trend of ΔZ_{Cr} as a function of saturation power is totally different. As illustrated by the phantom study for Cr in cross-linked BSA in Figure 4B and 4C, ΔZ_{Cr} drops rapidly for saturation powers higher than $1 \mu\text{T}$ (5 s saturation length), which is consistent with previous findings in both brain³³ and muscle.³⁴ Interestingly, the determined optimal saturation power ($1 \mu\text{T}$) for maximum effect was close to the one we observed ($1\text{--}1.2 \mu\text{T}$) in both mouse brain and muscle, which indicates that the Cr in cross-linked BSA phantom can mimic the in vivo Cr situation well. To illustrate the importance of MTC scale-down effects, Figure 8 shows simulations of the power dependence of CEST signal for four typical protons: protein guanidinium ($k = 30 \text{ s}^{-1}$), PCr ($k = 120 \text{ s}^{-1}$), Cr ($k = 900 \text{ s}^{-1}$) and protein amine ($k = 5000 \text{ s}^{-1}$) at an offset of 1.95 ppm at 11.7 T for the steady-state saturation, which represents a wide range of slow to fast-exchanging protons. The MTC and DS contributions, ie $R_{\text{eff}}+R_{\text{back}}$ values, were calculated according to Equation 16, while the R_{guan} values were determined from the theoretical power dependence^{39,44,60,61}

$$R_{\text{guan}} = \frac{fk(2\pi\gamma B_1)^2}{(2\pi\gamma B_1)^2 + k(k + R_{2b})} \quad (17)$$

where f is the concentration fraction relative to water for the exchanging proton, γ is the proton gyromagnetic ratio, and k and R_{2b} are the exchange rate and transverse relaxivity of the exchanging protons, respectively. Both $R_{\text{eff}}+R_{\text{back}}$ and R_{guan} increase with saturation power at low power levels (Figure 8A). However, while $R_{\text{eff}}+R_{\text{back}}$ and the relaxivity of fast-exchanging protons start to increase more rapidly with increasing saturation, the increase of R_{guan} plateaus for slower-exchanging protons. For example, for an R_{guan} of 30 Hz, the relaxivity rate levels off above $0.5 \mu\text{T}$. Hence, the observed CEST signal in the presence of MTC interference will drop rapidly when further increasing the saturation power, as shown in Figure 8B. This pattern perfectly matches the one we observed on the Cr + 20% BSA phantom (Figure 4C), mouse brain³³ and mouse muscle. From the simulation, we can see that the optimum saturation field is around $1.5 \mu\text{T}$ for the protons with exchange rates between 900 and 5000 Hz due to the strong MTC scaled-down effect. In our previous study on mouse brain,³³ we found that the ratio between the CEST signals from slow-exchanging protein guanidinium protons and much faster-exchanging Cr guanidinium protons at 1.95 ppm was saturation power dependent. This can be well explained by the simulation in Figure 8. At a saturation power of $0.5 \mu\text{T}$, the CEST signal from protein guanidinium protons reaches a maximum, while the CEST signal from Cr is relatively small. Hence, the guanidinium peak at 1.95 ppm is dominated by the CEST signal from protein guanidinium protons at lower power. With a further increase in saturation power, the CEST signal from protein guanidinium protons begins to decay, while the CEST signal from Cr is still in the process of building up. Between 1 and $2 \mu\text{T}$, the CEST signal from Cr dominates the guanidinium peak at 1.95 ppm with a ratio of around 0.5–0.8.

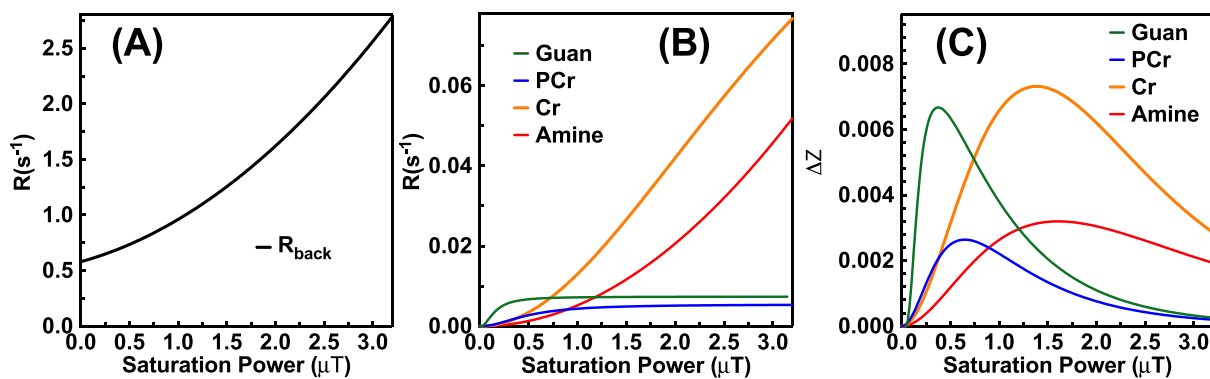


FIGURE 8 Illustration of the apparent relaxation terms from the background ($R_{\text{eff}}+R_{\text{back}}$) (a) and the apparent relaxation terms for four types of exchanging proton (R_{guan}) (b) as well as the corresponding observed CEST signal (ΔZ) as a function of saturation power (c). In this simulation, a strong MTC background (R_{back}) was included. The $R_{\text{eff}}+R_{\text{back}}$ term due to the combined water rotation frame relaxation (R_{eff}) and other saturation transfer effects (R_{back}) was calculated using equation 16 for mouse brain at 1.95 ppm. R_{guan} was calculated for four exchanging protons found at 1.95 ppm, namely protein guanidinium (guan) ($k = 30 \text{ s}^{-1}$, 7mM), PCr ($k = 120 \text{ s}^{-1}$, 5mM), Cr ($k = 900 \text{ s}^{-1}$, 5mM) and protein amine protons ($k = 5000 \text{ s}^{-1}$, 40mM) using equation 17 by assuming water $R_1 = 0.5 \text{ s}^{-1}$, $R_2 = 28.6 \text{ s}^{-1}$. Notice that the amine proton does not contribute to the CEST peak at 1.95 ppm, but contributes to the broad background at this offset. Here, we use the amine proton to demonstrate that MTC can significantly impact the CEST acquisition parameters for the fast-exchanging protons. The observed CEST signal was calculated using equation 10 with the $R_{\text{eff}}+R_{\text{back}}$ and R_{guan} values for each saturation power

5.2 | Saturation length selection

While many studies have been performed to optimize B_1 in the presence of strong MTC,^{5,37,38,62-65} to the best of our knowledge few studies have been carried out to optimize saturation length under a strong MTC effect. In most preclinical CEST studies, the saturation length has been chosen to reach steady state, which was believed to produce the maximum CEST signal. A relatively short saturation time (around 1 s) is often used in clinical studies, mainly due to the hardware limitations of clinical MRI scanners.^{66,67} The steady-state strategy is valid for the pure Cr solution as demonstrated in Figure 4A and 4C, but not in the presence of strong MTC. The maximum observed CEST signal may be reached at a shorter saturation time instead of at steady state, particularly when using higher saturation powers ($>1 \mu\text{T}$). This phenomenon can be well explained by the $R_{1\rho}$ theory in Figure 1 and was verified by the phantom study in Figure 5D and mouse brain in Figure 6F. When increasing the saturation length, both the MTC background and theoretical CEST signal are increasing, but the observed CEST signal is modulated by the scale-down effect (Equation 6) due to MTC competition, which may lead to suboptimal CEST signal in the steady state. According to Equation 6, the maximum observed CEST signal is reached at a saturation time slightly longer than $1/R_{1\rho}$. Compared with the results shown in Figures 5D and 6D, the improvement induced by optimizing saturation length is more obvious at high saturation powers with strong MTC interference, ie small Z^{ss} . This short saturation length optimum was also observed in the amine proton study using the chemical exchange-sensitive spin-lock (CESL) method with strong saturation powers.^{12,68} The short saturation length not only provides higher observed CEST signal, but also can reduce the repetition time (T_R) and total scan time. In addition, for clinical applications, the short saturation length can relieve the hardware requirements. It should be noted that the non-steady-state CEST signal (ΔZ_2 in Equation 8) is only significant when a small Z^{ss} is present due to the interference of either MTC, DS or a fast-exchanging competing CEST agent. With weak saturation powers ($<1 \mu\text{T}$), the CEST signal can still be approximated by a single exponential buildup function with respect to the saturation length (ΔZ_1 in Equation 7).

5.3 | In vivo CEST experiments

For in vivo CEST studies, it is common to see several exchanging protons at the same frequency offset, such as the guanidinium protons from proteins and Cr. The saturation power can be tuned to suppress the contributions from unwanted exchanging protons. Therefore, a high saturation power is helpful in suppressing the protein guanidinium signal as shown in Figure 8. However, high saturation power also causes severe scale-down effects due to MTC and DS, thus degrading the observed CEST signal. At low saturation powers ($<1 \mu\text{T}$), the CrCESTw peak was sharper (Figure 6E) but not consistent between the contralateral regions. This is because the sharp CEST line-shapes obtained with lower saturation powers not only are prone to the B_0 field inhomogeneity, but also can be easily disturbed by the B_0 fluctuation caused by animal respiration, motion^{69,70} and heating of the MRI shimming unit, which will lead to larger standard deviation as shown in Figure 6E. The above-mentioned issue can be addressed by applying a higher saturation power, as shown in Figure 6F. From the previous study,³³ the amide CEST signal is located between 3.2 ppm and 4 ppm at a saturation power of $2 \mu\text{T}$. Hence, the Z-spectral fit for CrCEST in this study was set to 1 ppm to 3 ppm to avoid potential interference from amide protons. From the theoretical prediction illustrated in Figure 8, the ΔZ of CEST peaks with relatively slow exchange rate decays rapidly with increasing saturation power. Although PCr has a similar concentration to Cr in mouse brain ($5.04 \pm 0.04 \text{ mM}$),⁷¹ PCr exhibits negligible CEST peak around 2.6 ppm for a saturation power of $2 \mu\text{T}$ due to its slow exchange rate ($140 \pm 50 \text{ s}^{-1}$)²⁵ (Figure 6F). This small dip from PCr can most likely not compete with the strong background MTC and DS assumed in PLOF. However, in the case where both strong PCr and CrCEST peaks exist, such as in Z spectra of skeletal muscle in which high concentrations of PCr exist (around 30 mM), the one-peak PLOF method used in this study may become invalid, and a two-peak PLOF method is required.³⁴ It should be pointed out that the PLOF method is not limited to quantification of PCr and CrCEST signals at high field, but is also suitable for other CEST contrasts with well defined CEST peaks even at low MRI fields, such as amide and PCrCEST at 3 T.⁷²

Combining the optimal saturation parameters and cryogenic cooled coil, a high-resolution Cr concentration map at an in-plane resolution of $230 \mu\text{m}$ could be obtained (Figure 7C). It is clear from Figure 7B that the ΔZ map is susceptible to the scale-down effect induced by MTC and DS, leading to an unclear but incorrect contrast between GM and WM. Compared with the ΔZ map, the Cr concentration map obtained via the PLOF method is more homogeneous across the brain, which is consistent with the previous studies by MRSI.^{73,74}

6 | CONCLUSION

In the current study, a systematic optimization was carried out for Cr mapping on mouse brain at 11.7 T using CEST MRI. The results indicated that competing strong MTC effects can dramatically impact the observed CrCESTw signal due to a scale-down effect, which can be well explained by the $R_{1\rho}$ theory. The maximum observed CrCESTw signal was reached at a short saturation time related to the rotating frame relaxation rate of MTC. The PLOF approach was therefore further developed to allow quantification of CrCESTw signal in the NSS and a high-resolution Cr concentration map was successfully obtained. The PLOF method developed in this study provides a simple and reliable way to quantify metabolite concentrations in the presence of strong background signals such as MTC.

ACKNOWLEDGEMENT

This work was supported by National Natural Science Foundation of China, 11474236.

FUNDING INFORMATION

Grant support: National Natural Science Foundation of China, 11474236.

ORCID

Shuhui Cai  <https://orcid.org/0000-0003-2767-9490>

Guanshu Liu  <https://orcid.org/0000-0002-8188-4332>

Hanzhang Lu  <https://orcid.org/0000-0002-3820-2391>

Jiadi Xu  <https://orcid.org/0000-0001-9698-5622>

REFERENCES

1. Sherry AD, Woods M. Chemical exchange saturation transfer contrast agents for magnetic resonance imaging. *Annu Rev Biomed Eng*. 2008;10(1):391-411.
2. van Zijl PCM, Yadav NN. Chemical exchange saturation transfer (CEST): what is in a name and what isn't? *Magn Reson Med*. 2011;65(4):927-948.
3. Liu G, Song X, Chan KW, McMahon MT. Nuts and bolts of chemical exchange saturation transfer MRI. *NMR Biomed*. 2013;26(7):810-828.
4. Zaiss M, Bachert P. Chemical exchange saturation transfer (CEST) and MR Z-spectroscopy *in vivo*: a review of theoretical approaches and methods. *Phys Med Biol*. 2013;58(22):R221-R269.
5. van Zijl PCM, Lam WW, Xu J, Knutsson L, Stanisiz GJ. Magnetization transfer contrast and chemical exchange saturation transfer MRI. Features and analysis of the field-dependent saturation spectrum. *Neuroimage*. 2018;168:222-241.
6. Jones KM, Pollard AC, Pagel MD. Clinical applications of chemical exchange saturation transfer (CEST) MRI. *J Magn Reson Imaging*. 2017;47:11-27. <https://doi.org/10.1002/jmri.25838>
7. Wolff S, Balaban R. NMR imaging of labile proton exchange. *J Magn Reson*. 1990;86:164-169.
8. Zhou J, Payen JF, Wilson DA, Traystman RJ, van Zijl PC. Using the amide proton signals of intracellular proteins and peptides to detect pH effects in MRI. *Nat Med*. 2003;9(8):1085-1090.
9. Zhou J, Lal B, Wilson DA, Lartera J, van Zijl PCM. Amide proton transfer (APT) contrast for imaging of brain tumors. *Magn Reson Med*. 2003;50(6):1120-1126.
10. Sun PZ, Zhou J, Sun W, Huang J, van Zijl PCM. Detection of the ischemic penumbra using pH-weighted MRI. *J Cereb Blood Flow Metab*. 2006;27(6):1129-1136.
11. Jia G, Abaza R, Williams JD, et al. Amide proton transfer MR imaging of prostate cancer: a preliminary study. *J Magn Reson Imaging*. 2011;33(3):647-654.
12. Jin T, Wang P, Zong X, Kim S-G. Magnetic resonance imaging of the amine-proton EXchange (APEX) dependent contrast. *Neuroimage*. 2012;59(2):1218-1227.
13. Li C, Peng S, Wang R, et al. Chemical exchange saturation transfer MR imaging of Parkinson's disease at 3 tesla. *Eur Radiol*. 2014;24(10):2631-2639.
14. Desmond KL, Moosvi F, Stanisiz GJ. Mapping of amide, amine, and aliphatic peaks in the CEST spectra of murine xenografts at 7 T. *Magn Reson Med*. 2014;71(5):1841-1853.
15. Cai K, Singh A, Poptani H, et al. CEST signal at 2ppm (CEST@2ppm) from Z-spectral fitting correlates with creatine distribution in brain tumor. *NMR Biomed*. 2015;28(1):1-8.
16. Chen LQ, Pagel MD. Evaluating pH in the extracellular tumor microenvironment using CEST MRI and other imaging methods. *Adv Radiol*. 2015;2015:206405.
17. Donahue MJ, Donahue PC, Rane S, et al. Assessment of lymphatic impairment and interstitial protein accumulation in patients with breast cancer treatment-related lymphedema using CEST MRI. *Magn Reson Med*. 2016;75(1):345-355.
18. Zhou J, Heo HY, Knutsson L, van Zijl PCM, Jiang S. APT-weighted MRI: techniques, current neuro applications, and challenging issues. *J Magn Reson Imaging*. 2019;50:347-364.
19. Chen L, Wei Z, Chan KWW, et al. Protein aggregation linked to Alzheimer's disease revealed by saturation transfer MRI. *Neuroimage*. 2018;188:380-390.
20. van Zijl PC, Jones CK, Ren J, Malloy CR, Sherry AD. MRI detection of glycogen *in vivo* by using chemical exchange saturation transfer imaging (glycoCEST). *Proc Natl Acad Sci U S A*. 2007;104(11):4359-4364.
21. Ling W, Regatte RR, Navon G, Jerschow A. Assessment of glycosaminoglycan concentration *in vivo* by chemical exchange-dependent saturation transfer (gagCEST). *Proc Natl Acad Sci U S A*. 2008;105(7):2266-2270.
22. Cai K, Haris M, Singh A, et al. Magnetic resonance imaging of glutamate. *Nat Med*. 2012;18(2):302-306.
23. Davis KA, Nanga RP, Das S, et al. Glutamate imaging (GluCEST) lateralizes epileptic foci in nonlesional temporal lobe epilepsy. *Sci Transl Med*. 2015;7(309):309ra161.
24. DeBrosse C, Nanga RP, Bagga P, et al. Lactate chemical exchange saturation transfer (LATEST) imaging *in vivo*: a biomarker for LDH activity. *Sci Rep*. 2016;6:19517.

25. Haris M, Nanga RP, Singh A, et al. Exchange rates of creatine kinase metabolites: feasibility of imaging creatine by chemical exchange saturation transfer MRI. *NMR Biomed.* 2012;25(11):1305-1309.
26. Haris M, Singh A, Cai K, et al. A technique for in vivo mapping of myocardial creatine kinase metabolism. *Nat Med.* 2014;20(2):209-214.
27. Zhang XY, Wang F, Afzal A, et al. A new NOE-mediated MT signal at around -1.6ppm for detecting ischemic stroke in rat brain. *Magn Reson Imaging.* 2016;34(8):1100-1106.
28. Chen L, Xu X, Zeng H, et al. Separating fast and slow exchange transfer and magnetization transfer using off-resonance variable delay multiple pulse (VDMP) MRI. *Magn Reson Med.* 2018;80(4):1568-1576.
29. Zu Z, Janve VA, Li K, Does MD, Gore JC, Gochberg DF. Multi-angle ratiometric approach to measure chemical exchange in amide proton transfer imaging. *Magn Reson Med.* 2012;68(3):711-719.
30. Zu Z, Janve VA, Xu J, Does MD, Gore JC, Gochberg DF. A new method for detecting exchanging amide protons using chemical exchange rotation transfer. *Magn Reson Med.* 2013;69(3):637-647.
31. Zu Z, Louie EA, Lin EC, et al. Chemical exchange rotation transfer imaging of intermediate-exchanging amines at 2 ppm. *NMR Biomed.* 2017;30(10):e3756. <https://doi.org/10.1002/nbm.3756>
32. Zhou IY, Wang E, Cheung JS, Zhang X, Fulci G, Sun PZ. Quantitative chemical exchange saturation transfer (CEST) MRI of glioma using image Downsampling expedited adaptive least-squares (IDEAL) fitting. *Sci Rep.* 2017;7(1):84.
33. Chen L, Zeng H, Xu X, et al. Investigation of the contribution of total creatine to the CEST Z-spectrum of brain using a knockout mouse model. *NMR Biomed.* 2017;30(12):e3834.
34. Chen L, Barker PB, Weiss RG, van Zijl PCM, Xu J. Creatine and phosphocreatine mapping of mouse skeletal muscle by a polynomial and Lorentzian line-shape fitting CEST method. *Magn Reson Med.* 2019;81(1):69-78.
35. Chung JJ, Jin T, Lee JH, Kim SG. Chemical exchange saturation transfer imaging of phosphocreatine in the muscle. *Magn Reson Med.* 2019;81(6):3476-3487.
36. Zhang XY, Xie J, Wang F, et al. Assignment of the molecular origins of CEST signals at 2 ppm in rat brain. *Magn Reson Med.* 2017;78(3):881-887.
37. Desmond KL, Stanisz GJ. Understanding quantitative pulsed CEST in the presence of MT. *Magn Reson Med.* 2012;67(4):979-990.
38. Zaiss M, Zu Z, Xu J, et al. A combined analytical solution for chemical exchange saturation transfer and semi-solid magnetization transfer. *NMR Biomed.* 2015;28(2):217-230.
39. Jin T, Autio J, Obata T, Kim S-G. Spin-locking versus chemical exchange saturation transfer MRI for investigating chemical exchange process between water and labile metabolite protons. *Magn Reson Med.* 2011;65(5):1448-1460.
40. Trott O, Palmer AG. $R_{1\rho}$ relaxation outside of the fast-exchange limit. *J Magn Reson.* 2002;154(1):157-160.
41. Trott O, Palmer AG III. Theoretical study of $R_{1\rho}$ rotating-frame and R_2 free-precession relaxation in the presence of n -site chemical exchange. *J Magn Reson.* 2004;170(1):104-112.
42. Yuan J, Zhou J, Ahuja AT, Wang YX. MR chemical exchange imaging with spin-lock technique (CESL): a theoretical analysis of the Z-spectrum using a two-pool $R_{1\rho}$ relaxation model beyond the fast-exchange limit. *Phys Med Biol.* 2012;57(24):8185-8200.
43. Moritz Z, Peter B. Chemical exchange saturation transfer (CEST) and MR Z-spectroscopy in vivo: a review of theoretical approaches and methods. *Phys Med Biol.* 2013;58(22):R221.
44. Zaiss M, Bachert P. Exchange-dependent relaxation in the rotating frame for slow and intermediate exchange—modeling off-resonant spin-lock and chemical exchange saturation transfer. *NMR Biomed.* 2013;26(5):507-518.
45. Xu J, Zaiss M, Zu Z, et al. On the origins of chemical exchange saturation transfer (CEST) contrast in tumors at 9.4 T. *NMR Biomed.* 2014;27(4):406-416.
46. Zaiss M, Xu J, Goerke S, et al. Inverse Z-spectrum analysis for spillover-, MT-, and T1-corrected steady-state pulsed CEST-MRI—application to pH-weighted MRI of acute stroke. *NMR Biomed.* 2014;27(3):240-252.
47. Roeloffs V, Meyer C, Bachert P, Zaiss M. Towards quantification of pulsed spinlock and CEST at clinical MR scanners: an analytical interleaved saturation-relaxation (ISAR) approach. *NMR Biomed.* 2015;28(1):40-53.
48. Windschuh J, Zaiss M, Meissner JE, et al. Correction of B1-inhomogeneities for relaxation-compensated CEST imaging at 7 T. *NMR Biomed.* 2015;28(5):529-537.
49. Ryoo D, Xu X, Li Y, et al. Detection and quantification of hydrogen peroxide in aqueous solutions using chemical exchange saturation transfer. *Anal Chem.* 2017;89(14):7758-7764.
50. Kim M, Gillen J, Landman BA, Zhou JY, van Zijl PCM. Water saturation shift referencing (WASSR) for chemical exchange saturation transfer (CEST) experiments. *Magn Reson Med.* 2009;61(6):1441-1450.
51. Zu Z, Lin E, Louie E, et al. Chemical exchange rotation transfer imaging of phosphocreatine in muscle. Paper presented at: Joint Annual Meeting ISMRM-ESMRMB 2018; Paris, France. 5106.
52. Tkac I, Henry PG, Andersen P, Keene CD, Low WC, Gruetter R. Highly resolved in vivo ^1H NMR spectroscopy of the mouse brain at 9.4 T. *Magn Reson Med.* 2004;52(3):478-484.
53. Mlynarik V, Cudalbu C, Xin L, Gruetter R. ^1H NMR spectroscopy of rat brain in vivo at 14.1 tesla: improvements in quantification of the neurochemical profile. *J Magn Reson.* 2008;194(2):163-168.
54. Kulak A, Duarte JM, Do KQ, Gruetter R. Neurochemical profile of the developing mouse cortex determined by in vivo ^1H NMR spectroscopy at 14.1 T and the effect of recurrent anaesthesia. *J Neurochem.* 2010;115(6):1466-1477.

55. Lei H, Poitry-Yamate C, Preitner F, Thorens B, Gruetter R. Neurochemical profile of the mouse hypothalamus using *in vivo* ^1H MRS at 14.1T. *NMR Biomed*. 2010;23(6):578-583.
56. Duarte JM, Lei H, Mlynarik V, Gruetter R. The neurochemical profile quantified by *in vivo* ^1H NMR spectroscopy. *Neuroimage*. 2012;61(2):342-362.
57. Provencher SW. Estimation of metabolite concentrations from localized *in vivo* proton NMR spectra. *Magn Reson Med*. 1993;30(6):672-679.
58. Provencher SW. Automatic quantitation of localized *in vivo* ^1H spectra with LCModel. *NMR Biomed*. 2001;14(4):260-264.
59. de Graaf RA, Brown PB, McIntyre S, Nixon TW, Behar KL, Rothman DL. High magnetic field water and metabolite proton T_1 and T_2 relaxation in rat brain *in vivo*. *Magn Reson Med*. 2006;56(2):386-394.
60. Meissner JE, Goerke S, Rerich E, et al. Quantitative pulsed CEST-MRI using Ω -plots. *NMR Biomed*. 2015;28(10):1196-1208.
61. Wu R, Xiao G, Zhou IY, Ran C, Sun PZ. Quantitative chemical exchange saturation transfer (qCEST) MRI—omega plot analysis of RF-spillover-corrected inverse CEST ratio asymmetry for simultaneous determination of labile proton ratio and exchange rate. *NMR Biomed*. 2015;28(3):376-383.
62. Kim J, Wu Y, Guo Y, Zheng H, Sun PZ. A review of optimization and quantification techniques for chemical exchange saturation transfer MRI toward sensitive *in vivo* imaging. *Contrast Media Mol Imaging*. 2015;10(3):163-178.
63. Zu Z, Li K, Janve VA, Does MD, Gochberg DF. Optimizing pulsed-chemical exchange saturation transfer imaging sequences. *Magn Reson Med*. 2011;66(4):1100-1108.
64. Zhao X, Wen Z, Huang F, et al. Saturation power dependence of amide proton transfer image contrasts in human brain tumors and strokes at 3 T. *Magn Reson Med*. 2011;66(4):1033-1041.
65. Kim B, So S, Park H. Optimization of steady-state pulsed CEST imaging for amide proton transfer at 3T MRI. *Magn Reson Med*. 2019;81(6):3616-3627.
66. Zhou J, Blakeley JO, Hua J, et al. Practical data acquisition method for human brain tumor amide proton transfer (APT) imaging. *Magn Reson Med*. 2008;60(4):842-849.
67. Heo HY, Zhang Y, Burton TM, et al. Improving the detection sensitivity of pH-weighted amide proton transfer MRI in acute stroke patients using extrapolated semisolid magnetization transfer reference signals. *Magn Reson Med*. 2017;78(3):871-880.
68. Jin T, Kim SG. Advantages of chemical exchange-sensitive spin-lock (CESL) over chemical exchange saturation transfer (CEST) for hydroxyl- and amine-water proton exchange studies. *NMR Biomed*. 2014;27(11):1313-1324.
69. Liu J, de Zwart JA, van Gelderen P, Murphy-Boesch J, Duyn JH. Effect of head motion on MRI B_0 field distribution. *Magn Reson Med*. 2018;80(6):2538-2548.
70. Wen J, Cross AH, Yablonskiy DA. On the role of physiological fluctuations in quantitative gradient echo MRI: implications for GEPCI, QSM, and SWI. *Magn Reson Med*. 2015;73(1):195-203.
71. Ljunggren B, Schutz H, Siesjö BK. Changes in energy state and acid-base parameters of the rat brain during complete compression ischemia. *Brain Res*. 1974;73(2):277-289.
72. Chen L, Schär M, Chan KKY, et al. High-resolution phosphocreatine mapping of human skeletal muscle using artificial neural network-based chemical exchange saturation transfer MRI at 3T. Paper presented at: 27th ISMRM Annual Meeting; May 13, 2019; Montreal, Canada. 0048.
73. Maudsley AA, Domenig C, Govind V, et al. Mapping of brain metabolite distributions by volumetric proton MR spectroscopic imaging (MRSI). *Magn Reson Med*. 2009;61(3):548-559.
74. Hangel G, Strasser B, Povazan M, et al. Ultra-high resolution brain metabolite mapping at 7 T by short-TR Hadamard-encoded FID-MRSI. *Neuroimage*. 2018;168:199-210.

How to cite this article: Chen L, Wei Z, Cai S, et al. High-resolution creatine mapping of mouse brain at 11.7 T using non-steady-state chemical exchange saturation transfer. *NMR in Biomedicine*. 2019;e4168. <https://doi.org/10.1002/nbm.4168>

APPENDIX A

For the situation where $R_{\text{guan}} \ll R_{\text{back}}$, the observed CEST signal ΔZ can be approximated by the following relation using Equation 5:

$$\Delta Z \approx -\frac{dZ}{dR_{1\rho}} R_{\text{guan}} \quad (\text{A1})$$

in which $dZ/dR_{1\rho}$ can be calculated from Equation 1, and is given by

$$\frac{dZ}{dR_{1\rho}} = -\frac{\cos^2 \theta R_1}{R_{1\rho}^2} (1 - e^{-R_{1\rho} t_{\text{sat}}}) - (1 - Z^{\text{ss}}) t_{\text{sat}} e^{-R_{1\rho} t_{\text{sat}}} \quad (\text{A2})$$

The observed CEST signal can be obtained by combining the above two equations:

$$\Delta Z \approx \frac{\cos^2 \theta R_1 R_{\text{guan}}}{R_{1\rho}^2} (1 - e^{-R_{1\rho} t_{\text{sat}}}) + (1 - Z^{\text{ss}}) R_{\text{guan}} t_{\text{sat}} e^{-R_{1\rho} t_{\text{sat}}}. \quad (\text{A3})$$

The steady-state CEST contrast ΔZ^{ss} (Equation 10) can be obtained by setting $t_{\text{sat}} = \infty$, ie

$$\Delta Z^{\text{ss}} = \frac{\cos^2 \theta R_{\text{guan}} R_1}{R_{1\rho}^2}. \quad (\text{A4})$$

At the steady-state saturation, the rotation frame relaxation term R_{guan} can be easily converted to its steady-state Z value ($Z_{\text{guan}}^{\text{ss}}$) based on Equation 2,

$$Z_{\text{guan}}^{\text{ss}} = \frac{\cos^2 \theta R_1}{R_{\text{eff}} + R_{\text{guan}}}. \quad (\text{A5})$$

Then, Equation A4 can also be described using Z^{ss} , $Z_{\text{guan}}^{\text{ss}}$ based on Equations 2 and A5:

$$\Delta Z^{\text{ss}} = Z^{\text{ss}2} \left(\frac{1}{Z_{\text{guan}}^{\text{ss}}} - \frac{1}{Z_{\text{DS}}^{\text{ss}}} \right). \quad (\text{A6})$$

$Z_{\text{guan}}^{\text{ss}}$ is the steady-state guanidinium Z spectrum when only guanidinium protons are present, and $Z_{\text{DS}}^{\text{ss}}$ is the water direct saturation without any exchanging protons. When the guanidinium signal is low, ie $1 - Z_{\text{guan}}^{\text{ss}} \ll 1$, and DS can be neglected, ie $Z_{\text{DS}}^{\text{ss}} = 1$, Equation A5 can be approximated by.

$$\Delta Z^{\text{ss}} \approx Z^{\text{ss}2} (1 - Z_{\text{guan}}^{\text{ss}}) \quad (\text{A7})$$

This equation was derived in our previous study.³³ It shows that the guanidinium signal ($1 - Z_{\text{guan}}^{\text{ss}}$) can be scaled down significantly ($Z^{\text{ss}2}$) in the steady state when strong MTC signal is present.